Australian Government
Department of Defence
Defence Science and
Technology Organisation

Establishment of a VISAR Measurement System for Material Model Validation in DSTO

A.D. Resnyansky, S.A. Weckert, A. Foord and C. Skibinski

Weapons Systems Division
Defence Science and Technology Organisation

DSTO-TR-2807

ABSTRACT

This report describes the establishment of a velocity interferometer measurement system, VISAR, capability in DSTO for recording high-temporal resolution velocity data in high-velocity impact experiments. This data is critical for model validation, material and warhead performance characterisation and effects studies. The present report describes preliminary plane impact tests used to establish the VISAR capability, and evaluates the methodological resolution issues relating to the experimental set-up. The set-up misalignment effects observed on the VISAR records have been numerically analysed using the CTH hydrocode and will be taken into consideration in future test programs.

Published by

Weapons Systems Division
DSTO Defence Science and Technology Organisation
PO Box 1500
Edinburgh South Australia 5111 Australia

Telephone: (08) 7389 5555
Fax: (08) 7389 6567

AR-015-538
February 2013

APPROVED FOR PUBLIC RELEASE

Establishment of a VISAR Measurement System for Material Model Validation in DSTO

Executive Summary

The Velocity Interferometer System for Any Reflector (VISAR) system is used extensively to provide a highly accurate measurement technique for recording the shock response of condensed materials. The system employs the well-known Doppler effect where the interference fringes of reflected light of a moving target are shifted in proportion to the target velocity. The system originates from the first advancements published in the works by L.M. Baker, E.R. Hollenbach and W.F. Hemsing [1-3] and results in the user-friendly interface and configuration of the VISAR system [4] used in the current work.

VISAR tests are among the mandatory instrumentation techniques when validating material models and establishing predictive capability using Finite-Element (FE) codes and hydrocodes. However, outsourced VISAR testing, where available, is prohibitively expensive due partly to the cost of the VISAR equipment but more so due to the cost of specially trained and experienced operators. Therefore, employment of an in-house VISAR system is beneficial and very economical.

Establishment of a VISAR capability in DSTO will allow the characterisation and analysis of material response to shock loads, including those loads due to warhead blast and fragmentation. This characterisation is of primary importance for the description of material response through constitutive material model refinement. Use of these models in hydrocodes advances the predictive capability. In addition, the VISAR test results can be used for the evaluation of target vulnerabilities and analysis of weapon efficiency.

The present work reports on preliminary tests using the recently commissioned DSTO VISAR system, providing an assessment of the experimental set-up and accuracy of the system installation. The effects associated with high strain rate material response and set-up projectile-target misalignment are analysed with the CTH code [5] using the rate sensitive model recently implemented in CTH [6]. Comparison of the simulation results with the test records from the VISAR system has demonstrated that the system is adequately capturing the material response with nanosecond resolution. These results indicate that the VISAR system is now ready for use in material and weapons effects studies.

References

1. Baker L.M. and Hollenbach R.E., Interferometer Technique for Measuring the Dynamic Mechanical Properties of Materials, Rev. Sci. Instr., 1965, v. 36, n. 11, pp. 1617-1620.
2. Baker L.M. and Hollenbach R.E., Laser Interferometer for Measuring High Velocities of Any Reflecting Surface, J. Appl. Phys., 1972, v. 43, n. 11, pp. 4669-4675.
3. Hemsing W.F., Velocity Sensing Interferometer (VISAR) Modification, Rev. Sci. Instr., 1979, v. 50, n. 1, pp. 73-78.
4. Barker L.M., Barker V.J., Barker Z.M., and Barker W.S., "Valyn VISARS User's Handbook", VALYN International, Albuquerque, New Mexico, USA, 2009.
5. Bell R.L., Baer M.R., Brannon R.M., Crawford D.A., Elrick M.G., Hertel E.S. Jr., Schmitt R.G., Silling S.A., and Taylor P.A., "CTH user's manual and input instructions version 7.1", Sandia National Laboratories, Albuquerque, NM, 2006.
6. Resnyansky A.D., Thermodynamically Consistent Decoupled Shear-Volumetric Strain Model and CTH Implementation, DSTO report, DSTO-TR-2299, 2009.

Authors

A. D. Resnyansky
Weapons Systems Division

Anatoly Resnyansky obtained a MSc in Applied Mathematics and Mechanics from Novosibirsk State University (Russia) in 1979. In 1979-1995 he worked in the Lavrentyev Institute of Hydrodynamics (Russian Academy of Science) in the area of constitutive modelling for problems of high-velocity impact. Anatoly obtained a PhD in Physics and Mathematics from the Institute of Hydrodynamics in 1985. He joined the Weapons Effects Group of the Weapons Systems Division (DSTO) in 1998. His current research interests include constitutive modelling and material characterisation at high strain rates, ballistic testing and simulation, and theoretical and experimental analysis of multi-phase flows. He has published over one hundred research papers and technical reports.

S. A. Weckert
Weapons Systems Division

Sam Weckert obtained a BE in Mechatronic Engineering from the Univeristy of Adelaide in 2004. He joined the Threat Mitigation Group of the Weapons Systems Division (DSTO) in 2004, and moved to the Weapons Effects Group in 2006. In 2010, he spent 6 months working in the high rate mechanics and failure branch at the Army Research Laboratory in the US. His current areas of work include warhead terminal effects modelling; instrumentation development; and material shock response and characterisation at high strain rates.

A. Foord
Weapons Systems Division

Andreas Foord joined the Weapons Effects Group in the Weapon Systems Division in 2010. Previous to that he had joined DSTO starting at SES (Scientific and Engineering Services) in 2006, before moving to the Weapon Systems Division in 2007. Prior to joining DSTO he worked within private industry for 5 years. He received an Advanced Diploma in Electronic Engineering from Regency TAFE SA in 2004. Since starting with the Weapons Effects Group he has been involved with electronic integration and assembly, ballistic instrumentation and high speed video.

C. Skibinski
Weapons Systems Division

Conrad Skibinski graduated from the University of Adelaide in 2011 with a BE in Aerospace and Mechanical Engineering. His involvement with DSTO projects include: conducting vulnerability and lethality assessments of various weapon and target systems, and assisting in the development of current experiments on material and warhead performance characteristics.

Contents

This page is intentionally blank

1. Introduction

The Velocity Interferometer System for Any Reflector (VISAR) system [1] has been used for a number of decades in high-velocity impact and explosively driven experiments for recording the free surface velocities of a target subject to shock wave loading.

In order to predict the shock response of advanced and emerging materials against a variety of blast and fragmentation threats, novel material models need to be validated using a high resolution instrumentation technique. The phenomenological response of alloys and filled glasses, composites and ultra high performance concretes critically involves the material effect of small aggregate components down to the nanometre scale. For example, advanced polymers, such as PTFE, have nanometre-sized amorphous and high-strength polymorph clusters affecting their phenomenological material response [2]. Therefore, analysis of the shock response of a material requires nanosecond resolution. This makes VISAR a highly suitable tool for this area of research.

The Weapons Systems Division (WSD) in DSTO recently acquired a VISAR system to conduct materials shock response research. As part of the system installation and commissioning process, several high-velocity impact tests, involving conventional materials, were conducted to verify the system performance. The corresponding VISAR records have been analysed using the rate-sensitive material model recently implemented by DSTO in the CTH hydrocode [3]. This model has been designed to predict the high-strain rate response of polymeric and conventional materials [4]. The currently employed stress decoupled adaptation of the model [5] in CTH is suitable for the analysis of various experimental test methodologies and plane impact geometries.

The experimental results presented in this report and the subsequent numerical analysis confirm that the current VISAR installation is capable of resolving processes on the nanosecond time scale and can be used for investigating relevant processes in advanced materials.

2. Gas gun set-up and VISAR experiments

The high-velocity impact tests in the present work were conducted using WSD's small gas gun materials test facility. The gas gun is a single stage system, utilising an intermediate chamber between two burster discs. Once the system is pressurised to the desired level the compressed gas in the intermediate chamber is vented to atmosphere, rupturing the burster discs and firing the gun [6]. This configuration enables controlled and repeatable firings. The present gas gun has a 3 litre breach which can be pressurised to a maximum firing pressure of 16 MPa and uses compressed air supplied from a dive air compressor.

The gas gun can be fitted with a variety of barrels. For the tests presented here a 30 mm smooth bore, slotted barrel of 2 m length was used. The rectangular keyway in the barrel prevents rotation of the projectile. This is advantageous for high velocity plate impact

experiments, where planar alignment of the impacting plate and target plate is critical to the success of the experiment. The alignment is checked prior to the experiment.

Two plate impact tests were conducted to commission the VISAR system. The test details are summarised in Table 1.

Table 1 Summary of the high-velocity impact experiments

Test #	**Flyer plate**	**Target plate**	**Impact velocity, U_0**
1	Aluminium 6061-T6	Aluminium 6061-T6	382 m/s
2	Steel 4140	Aluminium 6061-T6	365 m/s

The flyer plates were 5 mm thick, 27.65 mm diameter with an N6 (0.8 μm) surface finish on the impact face. The plates were held in a sabot machined from Delrin ® (acetyl homopolymer) plastic, shown in Fig. 1. The sabot was a two-piece design, with an insert for keying into the barrel slot to prevent rotation of the sabot-flyer plate assembly. The sabot dimensions were 29.7 mm diameter and 70 mm length. The flyer plate was set into the front of the sabot and, apart from a small support rim, had an air cavity behind it to provide a rear free surface for the flyer plate. This enabled the generation of a release wave from the reflection of the shock at the free surface during the impact event.

Figure 1 Sabot, 29.7 mm diameter and 70 mm length, made from acetyl homopolymer with an aluminium flyer plate

The target plates were 5 mm thick, 100 mm x 150 mm fabricated from a commercially available Aluminium 6061-T6 sheet. The impact face was neither machined nor polished, however, the rear surface was prepared with 400 grit sandpaper as recommended for optimum reflection for the VISAR probe. The target plates were clamped against a rigid stand inside a protective target trap at atmospheric air conditions.

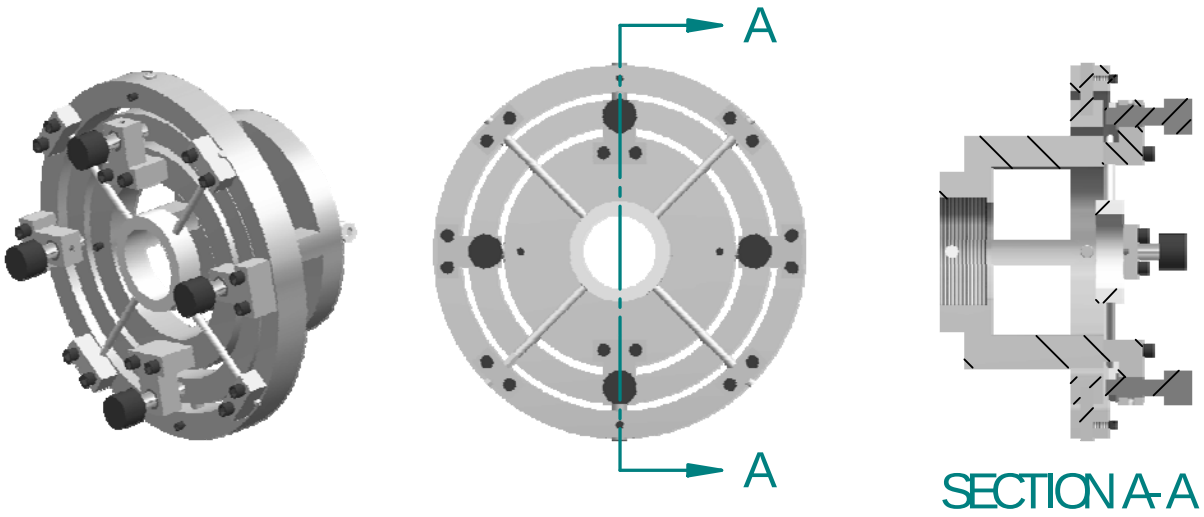

Figure 2 Details of the advanced target mount (general rear view, plane rear view, and side cross-section)

A more elaborate target holder based on a concept developed in [7] had been designed which mounted to the muzzle end of the barrel, as shown in Figs. 2-3.

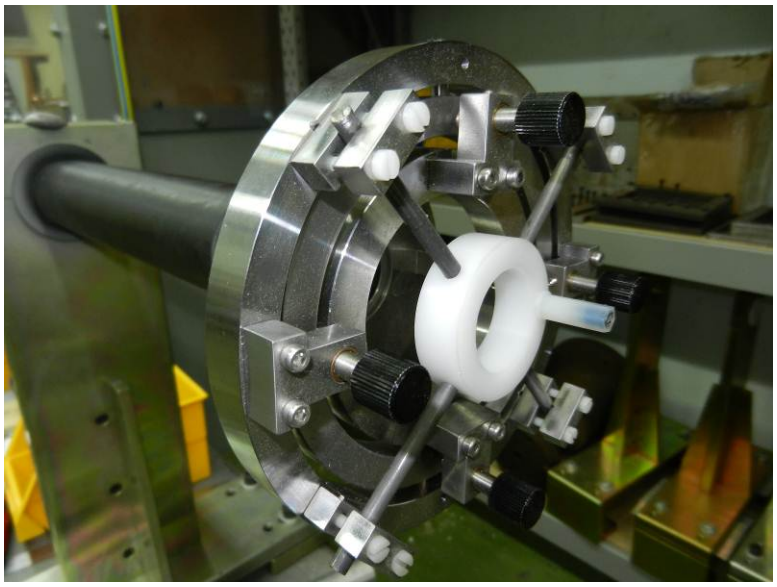

Figure 3 An advanced target mount (photograph)

The gimble arrangement allowed micro adjustment of the target impact interface for precise planar alignment with the flyer plate. In this configuration a disc target plate was held in a plastic holder support by four rods. The rods were designed to break during the impact event, protecting the delicate positioning screws. However, preliminary tests showed that this configuration requires a target trap with evacuated air to work effectively. When firing into the target assembly under atmospheric conditions, it was found that the target plate

orientation was significantly disturbed by the atmospheric air being pushed ahead of the projectile and expelled from the barrel. The air disturbance ahead of the flyer plate is initially acoustic and then becomes a shock once the projectile reaches supersonic velocity. This loading on the target plate prior to impact disturbs the impact planarity. Further stiffening of the supporting rods would help to limit the target plate movement; however, the risk is that significant loads are then transferred back to the delicate positioning screws which are used to allow for micro adjustment. It is anticipated that this set-up will be developed further and optimised once air evacuation in the target trap is realised.

Due to the pre-impact air loading, the rigid stand shown in Fig. 4 (left) was used to hold the target plates for the current tests. The projectile-target plate alignment was performed visually with the sabot-flyer plate positioned at the muzzle exit prior to conducting the test. Adjustment was performed by shimming the target plate against the rigid stand, down to 0.05 mm shim thickness. This set-up ultimately limited the ability to minimise impact planarity misalignment. However, the aim of this study was to verify installation and commission of the VISAR system. Establishing the VISAR technique was the highest priority, and therefore, the issue of impact planarity was of secondary concern.

The target plate mounting system incorporated into the rigid stand is shown in Fig. 4, where it is positioned in the gas gun target trap. Considering the possible sources of misalignment between the flyer and target plate due to the mounting system and un-machined target impact surface, it is expected that the tilt misalignment may be up to 0.1-0.2 mm. The effect of this degree of misalignment is investigated in the numerical analysis presented in Section 4.

Figure 4 Front and side views of the experimental set-up (target mount)

The VISAR fibre optic probe was held in a mounting bracket at the rear of the target. It was positioned concentrically with the barrel to within ±0.1 mm to measure the rear free surface velocity at the centre of the impacted area of the aluminium target material.

The instrumentation for the plate impact tests consisted of the following:

1. A velocity meter on the end of the barrel to measure the projectile velocity;
2. A high speed video camera for recording the impact event; and
3. The VISAR system for measuring the target rear free surface velocity.

The velocity of the sabot-flyer plate projectile was measured at the muzzle end of the barrel from the disruption of the beams produced by two photodiode emitter-receiver pairs. The first beam was located at 150 mm from the muzzle end, and the second beam at 50 mm; a spacing of 100 mm for calculation of the velocity. However, the current set-up may slightly under predict the impact velocity of the flyer plate against the target plate, as there are no venting holes or slots at the end of the barrel, prior to the velocity measurement. As a consequence, the projectile assembly may still be accelerating as it passes through the velocity meter and may not reach its final velocity until it has passed the velocity meter. Given the barrel length of 2 m and the length and position of the beams of the velocity meter, the expected error could be of the order of ± 5%.

The high-speed video footage of the event was recorded using a Photron SA5 high-speed camera. The camera recorded at 60,000 frames per second (approximately 16.7 μs between two subsequent frames), at 512 x 224 resolution, with a shutter speed at 1 μs. This fast shutter speed enabled sharp, blur free images, but necessitated the use of high output external lighting. A Palitte VIII ring light was used for illumination, using 8 x 300 W tungsten globes. The camera was triggered from the velocity meter which also provided the trigger for the VISAR data acquisition system.

The VISAR system, supplied by Valyn VIP, is a multi-beam VMBV-04 model. Currently the system includes two beam modules, which enables simultaneous velocity measurement of two points. The current VISAR system can be upgraded up to a maximum of seven modules. For these commissioning tests, only one beam module was used. The VISAR system was used together with a Coherent Verdi V6 laser, producing up to 6 W of 532 nm (green) laser light. In both tests, a Valyn plug and play fibre optic probe, with 30 mm focus and 5 mm depth of field, was used for illuminating the incident laser light and collecting the reflected light on the target rear face.

The principles of the VISAR operation are described in detail in the user manual [1]. Summarising briefly, the light from the laser travels through the fibre optic to illuminate the measurement point on the target. The light reflected from the target is frequency shifted by the target free surface velocity (the Doppler effect). This free surface velocity is caused by the shock wave arriving at the rear free surface. The reflected laser light is collimated and travels back through the fibre optic to the interferometer module where it is processed optically. The four quadrature light signal outputs from the interferometer travel through the fibre optic to the beam module where the light signal is converted by photomultiplier tubes, resulting in a voltage analogue signal. The voltage signals are processed and combined into two signal outputs by differential amplifiers. These outputs are then digitised and recorded by a suitable

data acquisition system and can be post-processed to give the velocity-time history at the measurement point with nanosecond resolution. Critically, this temporal resolution allows analysis of the reflected shock wave arriving at the target rear surface after travelling through the material. It provides information about the reflected wave structure and more broadly the material shock response.

For the current tests, the VISAR output signals were digitised and recorded using a Tektronix DPO7104C oscilloscope with sampling at 5 GS/s within 1 GHz bandwidth. For both tests, Etalons 2 and 3 [1] were installed in the delay leg of the interferometer, giving a velocity per fringe constant that was adequate for the expected free surface velocities. For Test 1, the 532 nm spike filter was not used in the interferometer and the laser was set to 100 mW to achieve optimum signal output. For Test 2, the spike filter was used and the laser set to 200 mW. The 532 nm spike filter necessitates using a higher laser power level, but it reduces noise in the optical signal in the interferometer and ultimately results in lower noise and improved signal fidelity of the measured velocity-time history.

3. High-speed photography and VISAR test records

High-speed video frames of the impact event are presented in Fig. 5, on the left, along with the corresponding graphically processed images of the sabots on the right. The side view of the flyer plate positioned at the front of the sabot is shown just after impact with the aluminium target plate.

Figure 5 Photographs of the projectile arriving at the target (left) along with graphically processed photographs of the sabots (right): a) Test 1 and b) Test 2

The sabots (white cylindrical bodies seen in Fig. 5) are deformed at the flyer plate end. The corresponding parts of the sabots are illuminated by the pyrophoric flash of the aluminium

target due to the projectile impact. The VISAR probes are seen behind the target at approximately 30 mm standoff from the rear surface, and opposite the centre point of the contact interface. It is seen by the shape of the flash at impact that the contact is reasonably simultaneous over the interface for both tests. However, a small asymmetry is noticeable confirming the assumption of misalignment between the flyer and target plates. This asymmetry is highlighted by the processed images (inversed colour with gradient contouring of the photograph images).

The impact velocity before impact can be evaluated from the high-speed photography images. However, from the spatial resolution (approximately 200 mm of the image resolved by 512 pixels) and temporal resolution (approximately 17 μs frame rate and 1 μs shutter speed), the velocity may be as much as 20% in error, resulting from resolving the distance between the end of the barrel and the target plate. Therefore, the velocity can be better determined from the velocity meter data, keeping in mind the velocity fluctuations after exiting the muzzle, as discussed previously.

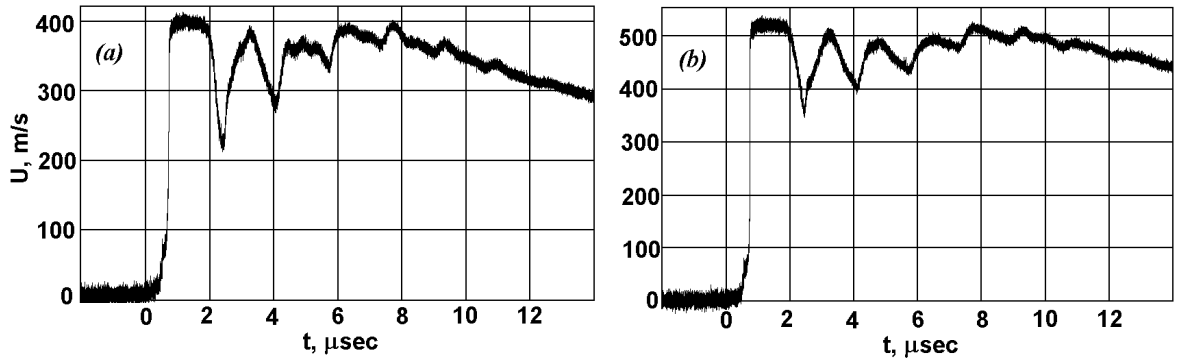

Figure 6 Summary of experimental data taken by the VISAR system for a) Test 1 and b) Test 2

The raw, unsmoothed VISAR data for Tests 1 and 2 are shown in Fig. 6. The observed time window in Fig. 6 exceeds possible influences from the lateral sides of the flyer plate originating at 2-3 μs after the flyer plate-target contact. Therefore, only the recorded information within this segment may correspond to the conditions of plane impact. Thus, the analysis is undertaken only for the 3 μs time window. Oscillation frequencies below 1 ns are not considered physically relevant. Therefore, the signal processing of the raw data involves a smoothing over a number of points.

The VISAR velocity profiles for the impact by the aluminium flyer plate (Test 1), averaged over 30 points, are shown in Fig. 7, and by the steel flyer plate (Test 2), averaged over 20 points, in Fig. 8.

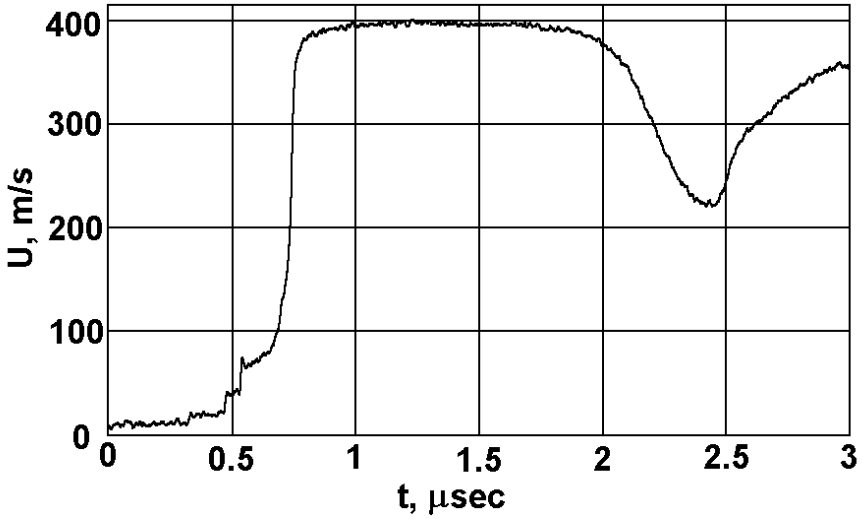

Figure 7 Experimental VISAR record of the free surface velocity of an aluminium target subject to high velocity impact by an aluminium flyer plate at impact velocity, U_0 = 382 m/s (Test 1)

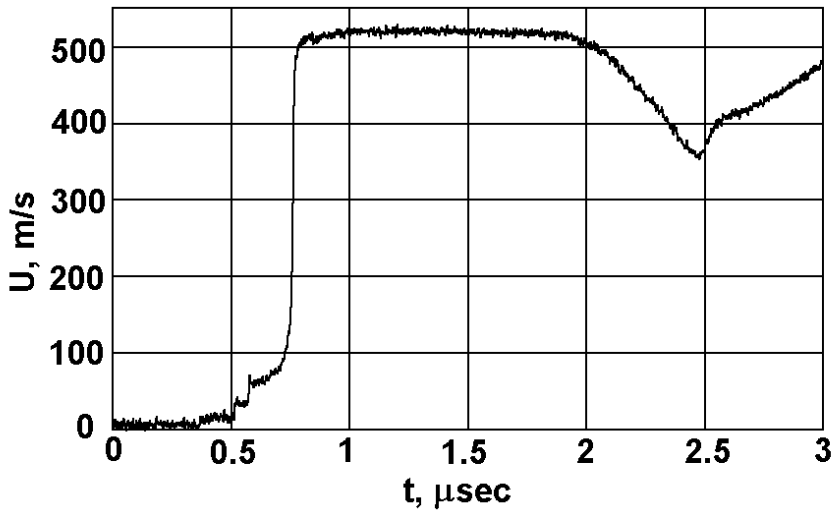

Figure 8 Experimental VISAR record of the free surface velocity of an aluminium target subject to high velocity impact by a steel flyer plate at impact velocity, U_0 = 365 m/s (Test 2)

For planar plate impact, the shock-wave interaction can be described by an (*x*-*t*)-diagram, in Fig. 9. For the flyer plate *F* impacting target *T*, occupying *x*-space 0 to 5 mm and 5 mm to 10 mm, respectively, the shock waves propagate left and right from the impact interface as shown. During propagation of these waves, the flyer plate decelerates from the initial impact velocity $U=U_0$ (state *1* of the (P-U)-diagram) and the target accelerates from the rest state *2* by left- and right-going shock waves, respectively, to state *3* with the same pressure and velocity at the projectile-target interface. These state transitions are described by Hugoniots H_F and H_T (for the flyer plate and the target, respectively), connecting the states in front of the shock waves and behind the waves. In the experiments, the impact velocities (U_0 = 382 m/s for Test 1 and U_0 = 365 m/s for Test 2) were sufficiently high to result in elastic-plastic transformation. This shock response is typical for aluminium and the transformation appears as a two-wave

splitting with the elastic precursor propagating ahead of the plastic shock wave. The splitting is observed in both tests, Figs. 7 and 8, and is discussed below.

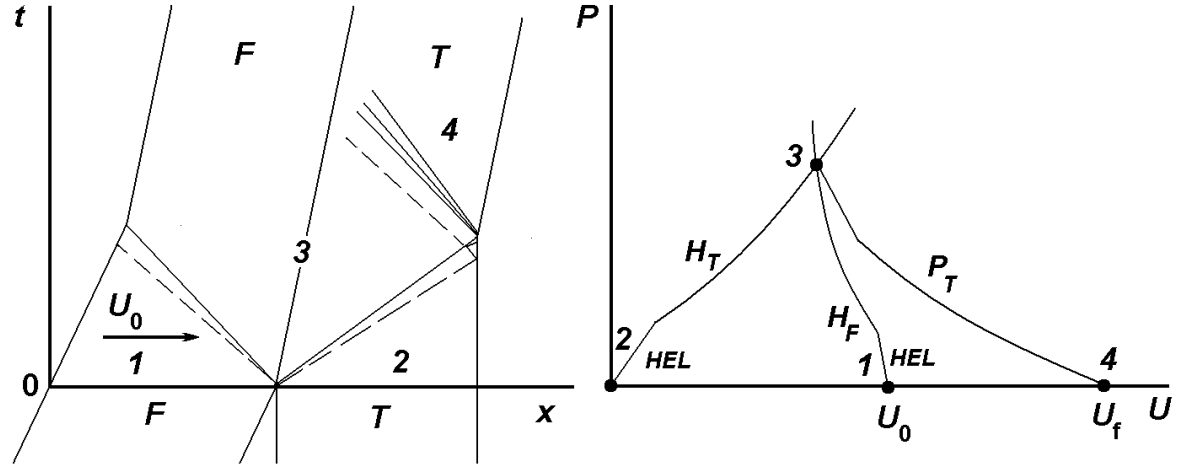

Figure 9 The (x-t)-diagram depicting impact of a target T by a flyer plate F with the impact velocity of U_0. The Hugoniots H_T and H_F describe the shock transitions 2-3 and 1-3 in the target and the flyer plate. The isentrope P_T describes the rarefaction transition 3-4 resulting in the free surface velocity U_f recorded by the VISAR.

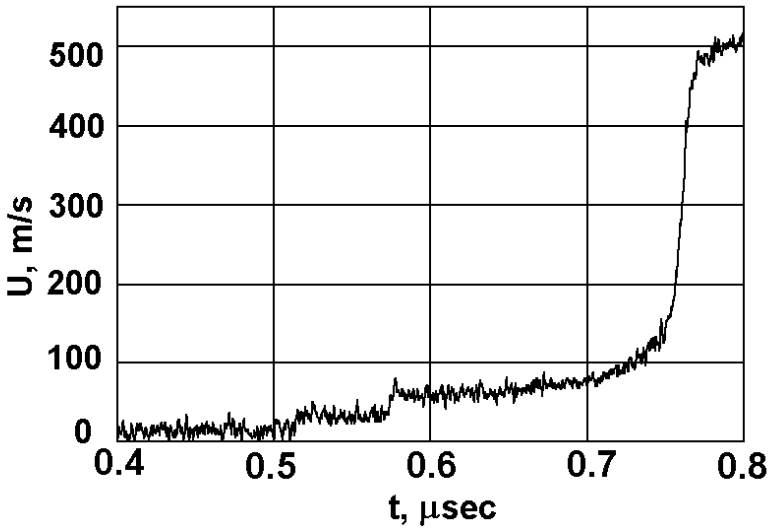

Figure 10 Magnified experimental VISAR record of the free surface velocity of an aluminium target subject to high velocity impact by a steel flyer plate at the impact velocity, U_0 = 365 m/s

The salient feature of the VISAR record of Test 2 is shown in Fig. 10, magnifying the portion of the shock front of Fig. 8 illustrating the extra splitting in the precursor wave. The same feature is also observed in the precursor part of Test 1, Fig. 7. A possible reason for this discrepancy from the expected wave shape will be discussed in the numerical analysed below.

4. Numerical simulations

Due to the apparent material strength effect observed as the elastic precursors in Figs. 7-8, the numerical simulation should incorporate an elastic-plastic material model. This material model should be rate-sensitive, such as the Steinberg-Guinan-Lund (SGL) model [8]. However, the SGL model involves a direct rate sensitivity dependence of the yield limit which adversely affects the thermodynamic consistency of the model. Current choices of constants in CTH for the SGL model for many materials (including steel and aluminium 6061-T6 alloy) have the rate sensitivity suppressed. Therefore, to address rate sensitivity effects, we use a model recently implemented in CTH by DSTO [5].

4.1 CTH input modification for the model

The implemented material model has the rate sensitivity of the yield limit realised via the shear stress relaxation mechanism (see [4, 5]). The key factor affecting the rate sensitivity of simulated conventional materials is the relaxation time function chosen in the following form [5, 9, 10]:

$$\tau(\rho, s, T) = \tau_0 \frac{\exp\left[\left(D_0 + H\varepsilon\right)/s\right]}{N_0 + M\varepsilon} \quad , \tag{1}$$

where s is determined from $s^2 = s_{ij} \cdot s_{ij}$, the second invariant of the stress deviator, $\varepsilon = Y/(4G)$ the deformation measure, τ_0, D_0, H, N_0, M are material constants and G is the shear modulus.

In order to facilitate the choice of constants in (1), an algorithm for fitting the constants as suggested in [9], has been used in this implementation and described in more detail in [11]. Summarising briefly, the user has to select two yield limit points, Y_1 and Y_2, at different strain rates, $\dot{\varepsilon}_1$ and $\dot{\varepsilon}_2$. The user also needs to select constants N_0 and M as an initial density and a multiplication factor for defects in the condensed material. With the present choice of parameter ε, H in (1) is redundant and is normally taken as $H = 0$. The idea of fitting constants τ_0 and D_0 in [9] is based on an approximation of the stationary solution of the viscoelastic model equations [4, 5]. It was observed in [9] that this solution is sufficiently close to the yield limit point. The stationary point of (1) can be found from [11]:

$$2G\dot{\varepsilon} = \frac{Y}{\tau} . \tag{2}$$

Substituting the dependence (1) into equation (2) and rearranging leads to the following equation

$$\ln\dot{\varepsilon} = \ln\frac{Y}{2G} - \ln\frac{\tau_0}{N_0} - \frac{D_0}{Y}\sqrt{\frac{3}{2}} + \ln\left(1 + \frac{M}{2N_0}\frac{Y}{2G}\right), \tag{3}$$

Using this equation it is possible to find τ_0 and D_0 when two pairs $\{Y_1,\ \dot{\varepsilon}_1\}$ and $\{Y_2,\ \dot{\varepsilon}_2\}$ are given. Usually, these data points are obtained experimentally from Split Hopkinson Pressure Bar (SHPB) compression tests.

Thus, the input data for the present model (VEM model from [5]) is introduced with the use of a modified UINEP.FOR subroutine in the CTH hydrocode. The modifications are read from the VP_data input file [5, 11, 12]. The corresponding material constants are: 'RHO', 'CL', 'B0', 'ALF0', 'BET0', 'GAM0', 'CV', 'ERT1', 'ERT2', 'Y1', Y2', 'H0', 'AN0', 'AM0'. A detailed description of the constants can be found in [5, 11].

These constants represent the following:
- initial density of porous material ρ – RHO;
- the longitudinal sound velocity l_0 – CL;
- the shear sound velocity b_0 – B0;
- the bulk modulus exponent a_0 – ALF0;
- the shear modulus exponent β_0 – BET0;
- the Grüneisen coefficient γ_0 – GAM0;
- the thermal capacity c_V – CV;
- $\log \dot{\varepsilon}$ related to the first test point – ERT1;
- $\log \dot{\varepsilon}$ related to the second point – ERT2;
- the yield limit Y_1 (Y in (2)) at compression, related to the first point – Y1;
- the yield limit Y_2 at compression, related to the second point – Y2;
- the hardening coefficient, H – H0;
- the initial defect density, N_0 – AN0;
- the defect multiplication coefficient, M – AM0;

It should be noted that the model uses non-standard units for CTH input of *cm* (length), *g* (mass), 10 μs = 10^{-5} s (time), and ^{o}K (temperature). The strain rate $\dot{\varepsilon}$ for ERT1 and ERT2 is taken in inverse seconds, s^{-1}. The derived pressure in these units is GPa.

4.2 Numerical Results

The effects of the surface defects and non-planarity between the flyer plate and target on the VISAR measurements are analysed numerically here. The calculations are performed using the CTH hydrocode with the material model [5]. Input for this model is described in the previous subsection.

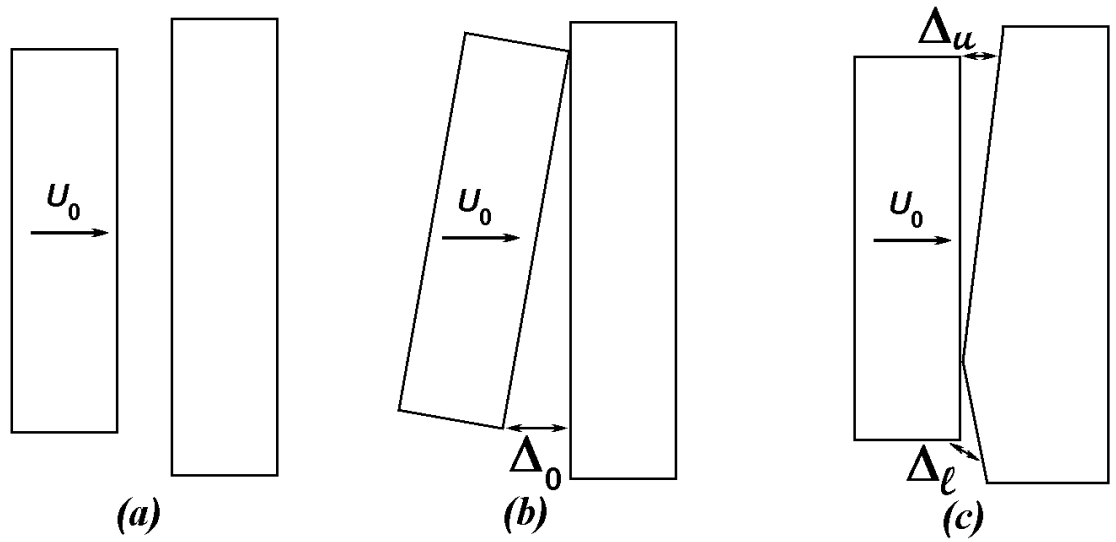

Figure 11 The flyer plate-target set-ups considered for numerical analysis to assess the effects of non-planarity and surface defects at impact. Planar impact (ideal) (a); impact by a tilted flyer (b); and impact against a bulged target (c).

The geometries considered for the numerical analysis are shown schematically in Fig. 11. The straightforward case of planar impact is shown in Fig. 11(*a*). Unfortunately, this is the only case that can be analysed within a one-dimensional numerical set-up. The case of a tilted flyer plate (or imperfect positioning of a perfectly flat target plate) is shown in Fig. 11(*b*). Finally, an approximation of the case of a bulged target (or a target with imperfect surface) is shown in Fig. 11(*c*). The number of geometries is significantly larger when considering three dimensions, however, for the sake of simplicity we limit our consideration to the cases above. The impact misalignment in the second case can be characterised by the maximal distance Δ_0 from a point on the flyer plate to the target when the opposite point of the flyer plate contacts the target (Fig. 11(*b*)). The imperfection in the last case can be characterised by a number of parameters, namely, the distances between the flyer plate and the target at the upper and lower points, Δ_u and Δ_l, respectively, when the flyer plate contacts the target at some point; and the respective vertical coordinate of this contact point (the set-up may be symmetrical, if the contact point is coincident with the centre of the projectile and $\Delta_u = \Delta_l$) or asymmetrical (as shown in Fig. 11(*c*)). These two last cases can only be analysed using 2D or 3D geometries.

The first case considered will enable a comparison with the VISAR record. This will involve a 1D analysis of Fig. 11(*a*), where the lateral dimensions are infinite in this case.

4.2.1 One-dimensional calculations of ideal planar impact

The one-dimensional calculations have been conducted using CTH with the VEM model [5]. These calculations were also compared with results obtained by an in-house code based on the Godunov adaptive mesh method [13], resulting in an Arbitrary Lagrangian-Eulerian (ALE) code. The materials used in the calculations are steel and aluminium. The choice of steel material constants is not critical for the shock wave transmitted through the target provided that the impedance mismatch between the flyer and target materials is correct. Therefore, for

the steel material, input data for the constants described in subsection 4.1 are taken from [5], namely,

ρ = 7.84 g/cm^3, K = 168.3 GPa, G = 64.4 GPa, Y_1 = 0.22 GPa, Y_2 = 0.44 GPa,

a_0 = 0.635, β_0 = 1.6917, γ_0 = 1.6723, c_V = 0.45 J/g/grad, $N_0 = 10^6$, $M = 10^{11}$.

The constants corresponding to the aluminium 6061-T6 alloy are:

ρ = 2.703 g/cm^3, K = 73.65 GPa, G = 27.6 GPa, Y_1 = 0.2 GPa, Y_2 = 0.25 GPa,

a_0 = 1.078, β_0 = 2.577, γ_0 = 1.97, c_V = 1.07 J/g/grad, $N_0 = 10^6$, $M = 10^{10}$.

The yield limits are chosen at strain rates of $\dot{\varepsilon}_1 = 10^{-2}$ s^{-1} and $\dot{\varepsilon}_2 = 10^3$ s^{-1}. The bulk and shear moduli K and G, respectively, are linked with the sound velocities l_0, b_0, and the bulk sound velocity, c_0, as follows:

$K = \rho c_0^2$, $G = \rho b_0^2$, $c_0^2 = l_0^2 - 4b_0^2/3$.

The first calculation, using the constants above, has been conducted employing the in-house code.

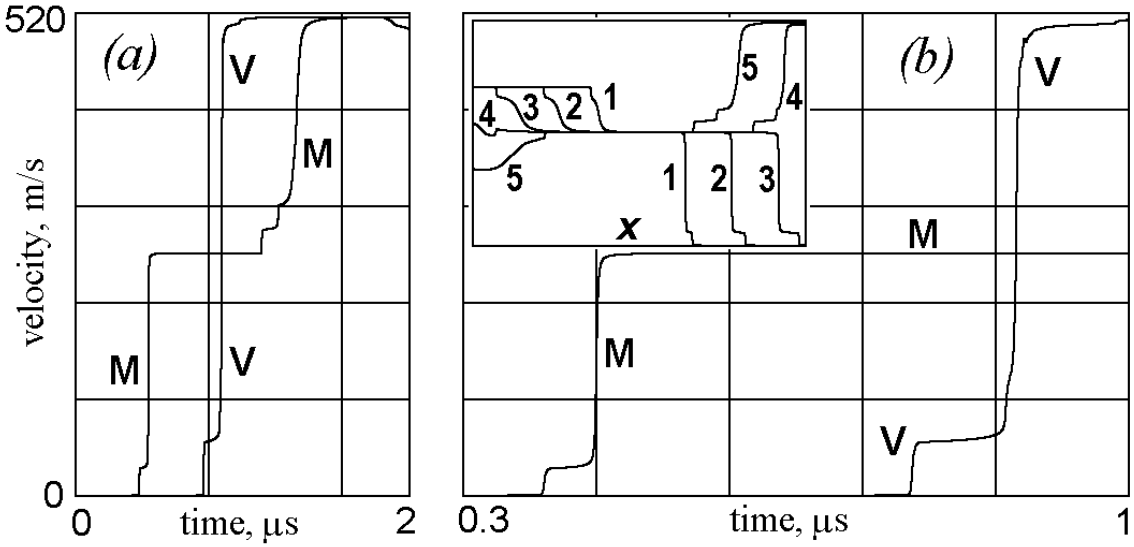

Figure 12 One-dimensional calculation of the high-velocity impact of an aluminium target by a steel flyer plate at impact velocity, U_0 = 365 m/s using the in-house ALE code. The velocity-time profiles M in the middle of the target are plotted along with the profiles V at the free surface of the target. Velocity profiles inside the flyer plate-target assembly are drawn in the insert of the graph (b) at every 0.25 μs of the profile evolution.

The calculation results of the planar high-velocity impact of a steel flyer plate against an aluminium target at U_0 = 365 m/s (Test 2) are shown in Fig. 12. The calculation has been conducted on a fine mesh, grid size $\Delta x = 6.25 \cdot 10^{-3}$ mm, which provides very accurate

resolution of the tracer information. The tracers are Lagrangian points in the middle of the target at x = 2.5 mm from the flyer plate-target impact interface noted by M; and at x = 5 mm from the interface at the target free surface noted by V. This information is accurate because the adaptive mesh used in this calculation resolves the contact and free interfaces as well as additional interfaces in the Lagrangian frame, whereas the remaining internal nodes are Eulerian [13]. Thus, no numerical erosion occurs at the tracer coordinates. Here, the extra interface of choice refers to the middle interface, introduced to resolve the Lagrangian tracer in the middle of the target.

The calculation results presented as the tracers V and M for the 2 μs-time frame are shown in Fig. 12(*a*) and in more detail in the vicinity of the shock front in Fig. 12(*b*). The insert velocity-space graphs in Fig. 12(*b*) represent the velocity profiles within the projectile-target assembly, taken at 0.25 μs intervals. It should be noted that the profiles are scaled back into the original coordinate system to aid visualisation.

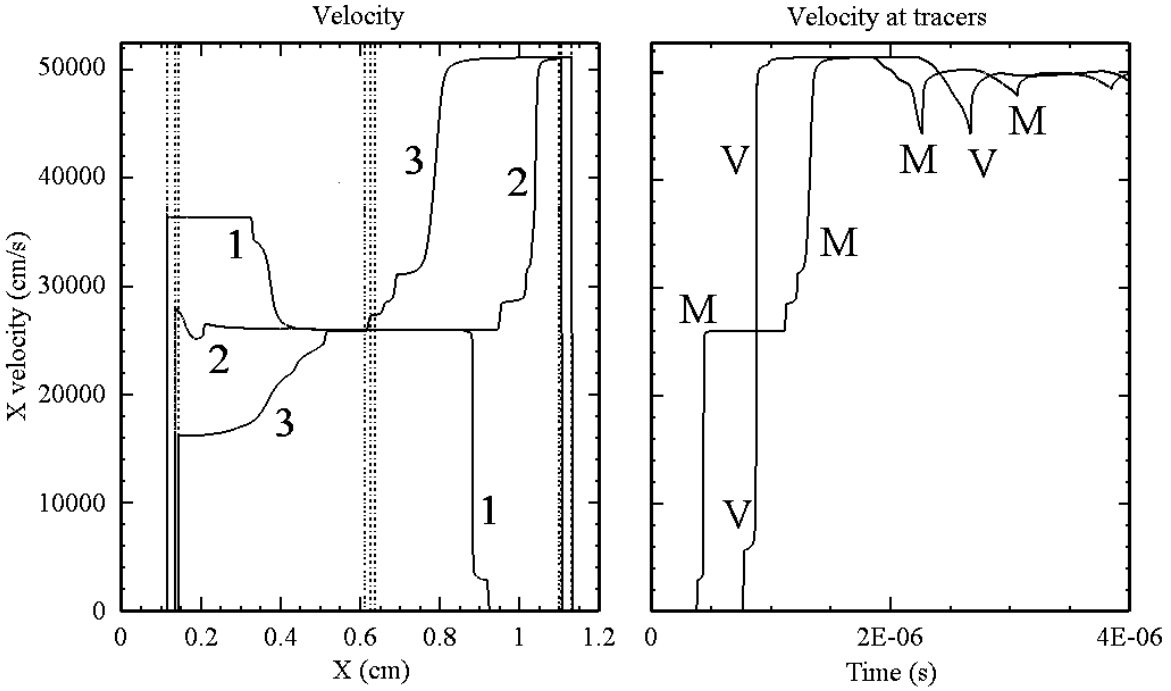

Figure 13 1D CTH calculation on a very fine mesh showing the velocity profiles within the flyer plate-target assembly every 0.5 μs, the velocity at tracers in the middle of the target (M - tracer 1) and at the free surface (V - tracer 3). The viscoelastic model implemented in CTH is employed in this calculation for the impact of an aluminium target by a steel flyer plate at impact velocity, U_0 = 365 m/s.

The results of the CTH calculation with the VEM model for the same geometry are shown in Fig. 13. The calculation has been conducted on a very fine mesh, grid size $\Delta x = 3.125 \cdot 10^{-3}$ mm. The left section of the graph represents the velocity profiles inside the flyer plate-target assembly, similar to the insert graph in Fig. 12(*b*). The profiles are plotted and taken at 0.5 μs intervals. The right section shows the velocity at the tracers M and V, as above, for the full 4 μs-length calculation. The major difference of these velocity-space profiles, in contrast to the

previous ones, is the moving interface and free surfaces, indicated by the dashed vertical lines due to this fully Eulerian calculation.

It seems that both numerical results are in a reasonable agreement. A few features from the tracers and velocity profiles within the materials are worthy of comment. The first one that is obvious is the propagation of the elastic precursor ahead of the plastic shock front. The velocity behind the precursor, as seen in the both calculations and in both the tracer velocity and velocity-space profiles, evolves with a small but noticeable increase in amplitude along the precursor. This increase demonstrates the rate sensitivity of the yield limit in this model. Another feature is the multiple wave structure in the reflected wave (profiles 4 and 5 in Fig. 12(*b*) and profile 2 in Fig. 13). This additional wave is a well-known effect and results from the interaction of the elastic precursor reflected from the free surface with the incoming plastic shock wave (the transition zone between states *2* and *4* near the free surface of target *T* shown in the (*x*-*t*)-diagram in Fig. 9).

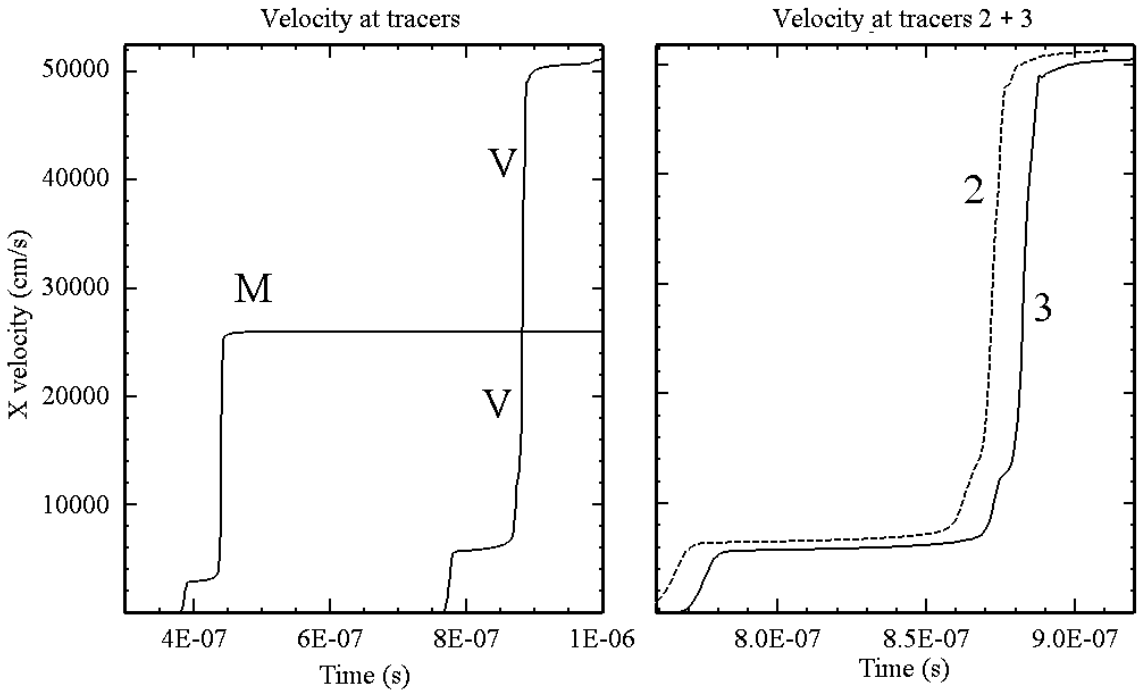

Figure 14 Velocity at tracer 1 - M and tracer 3 - V (on the left of the plot) for the CTH calculation on a very fine mesh using the viscoelastic model. Velocity at tracer 2 (dashed profile shifted down in time and up in amplitude) and tracer 3 (solid profile) on the right.

This interaction effect is seen in the free surface tracer V as an additional 'wave splitting' of the reflected wave behind the elastic precursor in the tracer V in Fig. 12(*b*). It is difficult to discern this effect in the 4 μs-trace of the CTH calculation in Fig. 13. However, by magnifying the time base, this effect becomes prominent in the left section of Fig. 14, whereas there is no such effect observed in the incoming wave itself (tracer M). The tracer V can be further scaled to make this feature even more noticeable in the right section of Fig. 14 (this tracer has its own marking in the CTH run as tracer 3). It should be noted that this calculation is Eulerian.

Therefore, another tracer is added into the CTH calculations (tracer 2) that is in close vicinity to the free surface. It is located at x = 4.9 mm from the projectile-target interface and, correspondingly, 0.1 mm away from the free surface. The purpose of comparison of the velocities at tracers 2 and 3 is to control the numerical effects and evaluate the effect of the surface erosion when the target material is expanding to the numerical 'void' area [3]. The velocity at tracer 2 is shown in Fig. 14 by the dashed line and is virtually coincident with the velocity at tracer 3 (solid line) in both the time and the velocity amplitude. In order to see the difference clearly, the tracer 2 curve has been shifted slightly to the left and raised. The comparison reveals a slight smearing of the 'bulge' feature behind the precursor for tracer 2 and a slight smearing of the plastic wave at the velocity amplitude near its maximum. In general, the tracer 3 profile is quite close to that for the in-house calculation in Fig. 12.

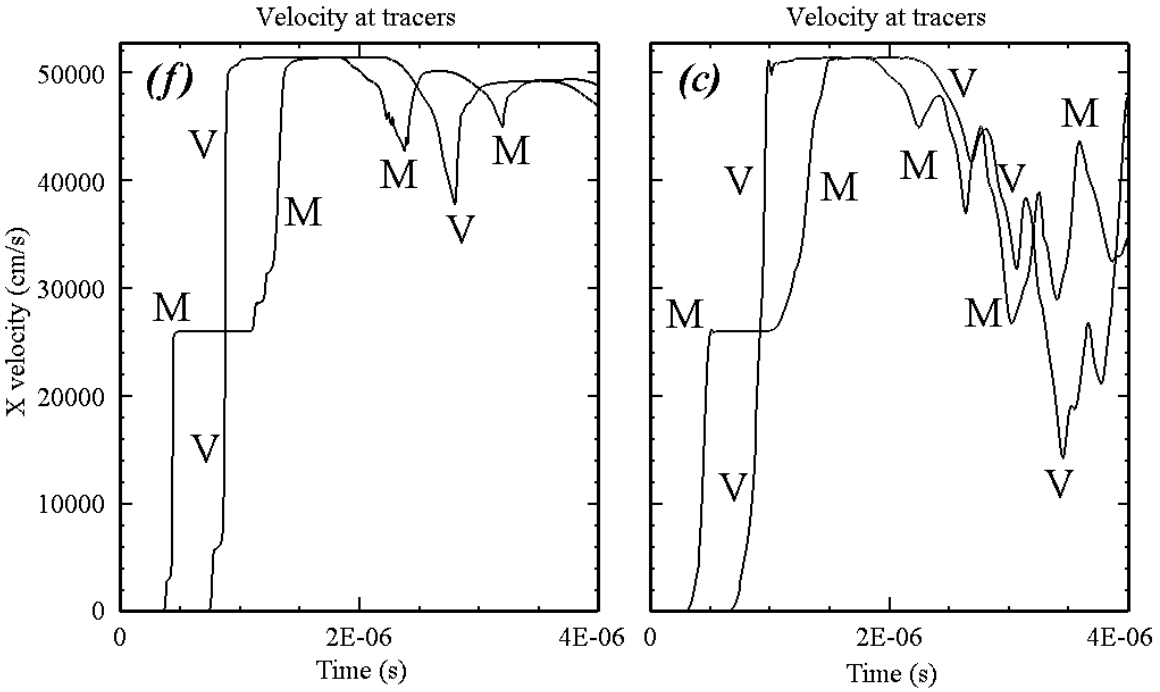

Figure 15 Velocity at the tracers M and V from the one-dimensional CTH calculation on a fine, (f), and coarse, (c), meshes

To observe the solution convergence, two additional calculations have been conducted on meshes with $\Delta x = 1.25 \cdot 10^{-2}$ mm (fine mesh) and Δx = 0.12 mm (coarse mesh). The results of these calculations are presented in Fig. 15. Comparison of these calculations with those on a very fine mesh (Fig. 14) demonstrates that the fine mesh calculation has converged, whereas the coarse mesh calculation has not. In particular, the latter poorly resolves the three-wave structure of the wave reflected from the target's free surface. Indeed, the structure observable after 1 μs on tracer M in Fig. 15(*f*) is not seen on the same tracer in Fig. 15(*c*). In addition, the free surface velocity increase occurring after 2 μs due to the separation of the target from the flyer plate, agrees reasonably well with the previous calculation and experiments. Whereas, the coarse mesh calculation produces uncontrolled velocity oscillations on the free surface after the separation.

4.2.2 Three-dimensional calculation of the tilted flyer plate

To observe the effects of misalignment due to tilt between the impacting flyer plate and target plate, the following 3D calculation has been performed. The calculation uses the same material model and constants as the 1D CTH calculations in the previous section.

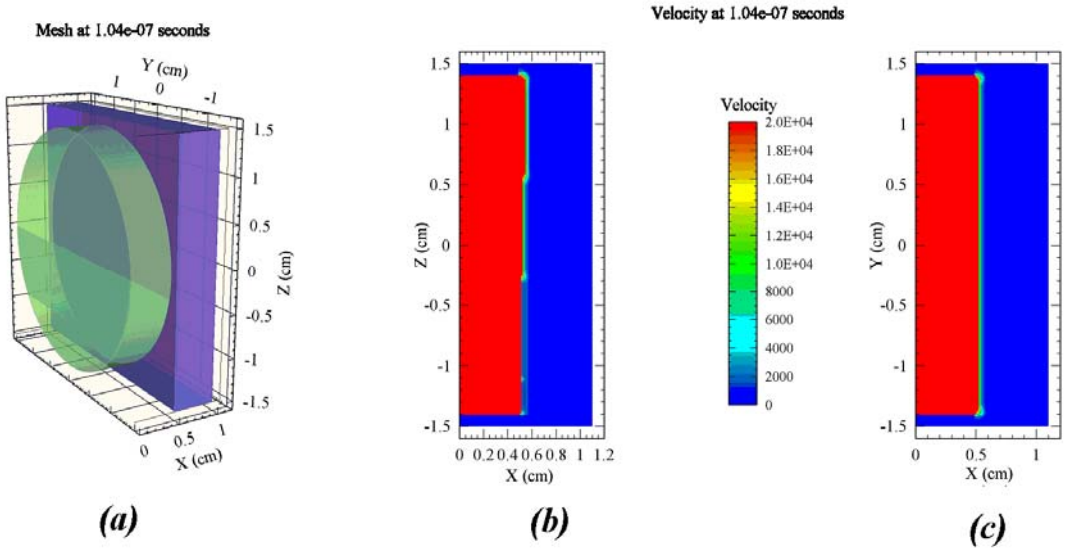

Figure 16 3D CTH viscoelastic model calculation of the high-velocity impact of an aluminium target by a steel flyer plate, with maximum misalignment gap of 0.05 mm, at impact velocity, U_0 = 365 m/s. General view of the flyer plate partially contacting the target (a) and velocity distributions at the assembly cross-sections y = 0 (b) and z = 0 (c).

The geometry for the 3D calculation presented here is physically very close to the real geometry in Test 2 of the VISAR commissioning experiments. A steel flyer plate impacts an aluminium target plate at velocity, U_0 = 365 m/s. The flyer plate diameter is 28 mm and the thickness is 5 mm and the target thickness is also 5 mm. Shock waves due to the impact are primarily perpendicular to the impact face, directed along the *x*-axis. For the numerical set-up the centre point of the flyer-target impact interface passes through the $y = z = 0$ line. A slight tilting of the flyer plate is introduced such that the configuration of the flyer-target assembly cross-sectioned by the $y = 0$ plane is schematically represented by the configuration shown in Fig. 11(*b*). The degree of misalignment defined in Fig. 11(*b*) as Δ_0, is chosen to be $\Delta_0 = 0.05$ mm.

The assembly geometry and velocity fringes for this set-up are shown in Fig. 16 at the beginning of the projectile-target interaction at $t = 0.1$ μs. It is seen in Fig. 16(*a*) that the flyer plate is partially contacting the target, appearing as the darker interaction area on the projectile-target contact interface.

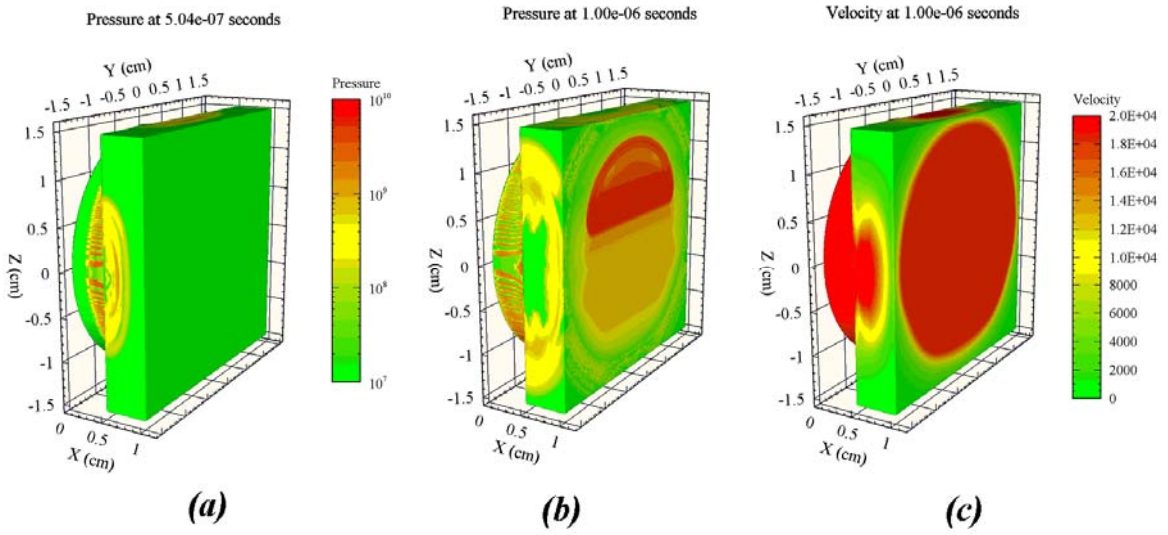

Figure 17 Calculated pressure and velocity distributions in the assembly illustrating the vertical misalignment

The velocity fringes at the assembly cross-sections, for the planes $y = 0$ (Fig. 16(*b*)) and $z = 0$ (Fig. 16(*c*)) passing through the interface centre point, show that the tilting introduces asymmetry for the first velocity distribution and it is symmetrical for the latter one. This asymmetry effect propagates with time along the *x*-axis.

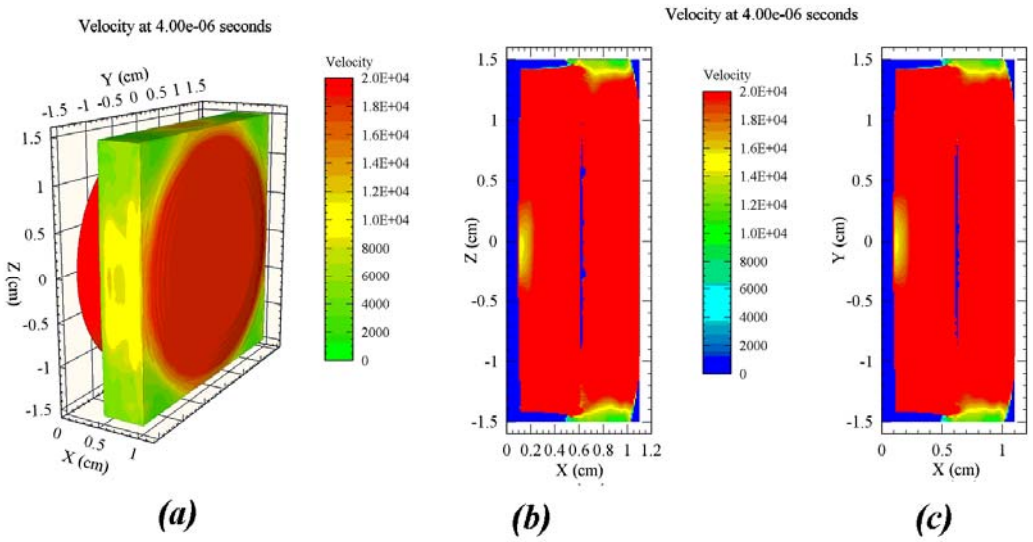

Figure 18 Calculated velocity distributions in the assembly after the flyer plate-target separation illustrating the numerical effects of the separation process

When approaching the target's free surface this asymmetry results in the variable pressure and velocity distributions along the z-axis as shown in Figs. 17(*b-c*) at $t = 1$ μs. The latter appears at the rear free surface of the target in Fig. 17(c) as a non-circular zone of a high free

surface velocity. The pressure variable, a combination of stress components, is used in the graphic plots of this subsection for illustration of the shock wave circulation.

The 3D calculation presented here could only be conducted on a fairly coarse mesh due the memory restrictions for the single-CPU version of CTH. Numerically, the spatial discretization of this mesh, 0.12 mm in each of the three dimensions, corresponds to the 'coarse' mesh 1D calculation of the previous subsection. The numerical dissipation results in the erosion effects seen on the velocity distribution graphs in Figs. 18(*b*-*c*). These numerical effects occurring at the flyer plate-target separation result in a non-smooth separation interface with associated effects on the velocity tracers 2 μs after the beginning of the interaction.

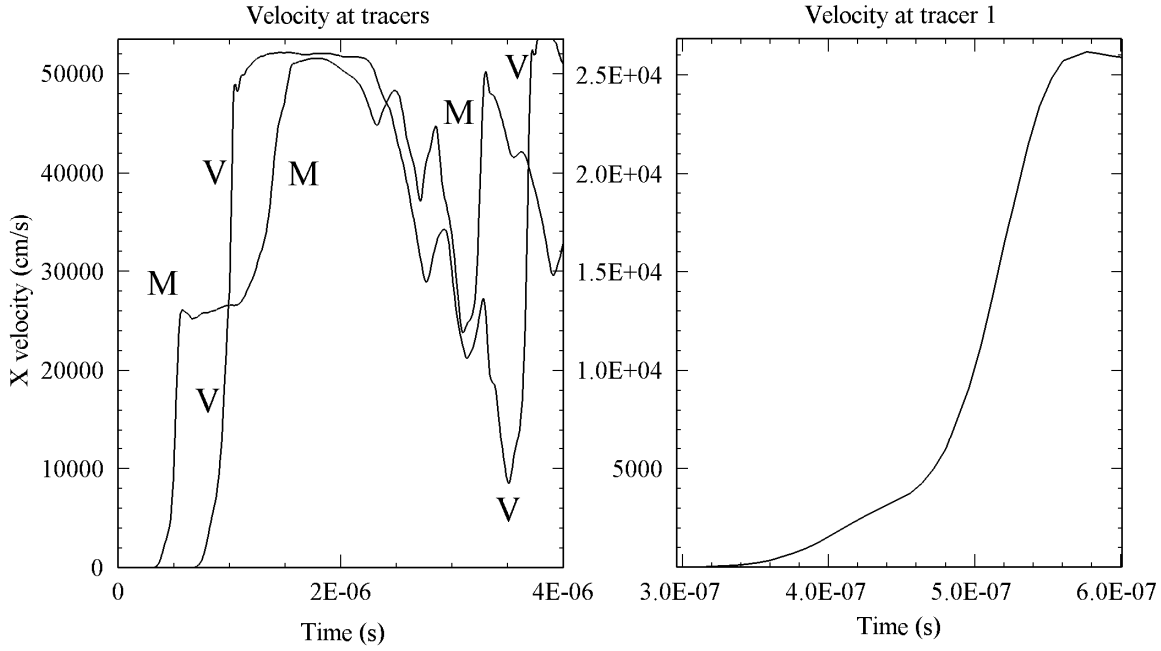

Figure 19 Velocity tracers in the middle (M) and at the free surface (V) of the target for the 3D CTH calculation. The detailed view (the right plot) of tracer 1, located in the middle of the target, illustrates the achievable numerical resolution for the three-dimensional calculation.

The corresponding velocity tracers were taken at $y = z = 0$ line from the same x-points as in the previous subsection and are shown in Fig. 19. The uneven plateau where the velocities at tracers M and V approach their maximum (after the flyer plate-target separation) demonstrates the dissipation effect of the mesh. To observe the calculated wave structure in detail, the time base for velocity tracer M (tracer 1 in the run) has been expanded and is shown in the right plot of Fig. 19. This plot demonstrates that the spatial resolution of the 3D calculation is not sufficient to observe any relevant features in the shock wave structure with the exception of a rough contour of the elastic precursor. Therefore, for a more rigorous analysis we concentrate on the two-dimensional calculations in the subsection below. For the geometrical misalignment effects in the vertical direction, two-dimensional calculations cannot embrace the side effects due to free surfaces in the y-direction but they can at least take into account the vertical-direction misalignment effects. Unfortunately, from the present

subsection analysis, possible 3D geometry imperfections and misalignments cannot be analysed. However, our main objective is to assess if any set-up imperfections at all (even within the two-dimensional set-up) may explain some features of the observed experimental VISAR records.

4.2.3 Two-dimensional calculations of aligned and misaligned assemblies

The 2D geometries considered below correspond to all three cases illustrated in Fig. 11.

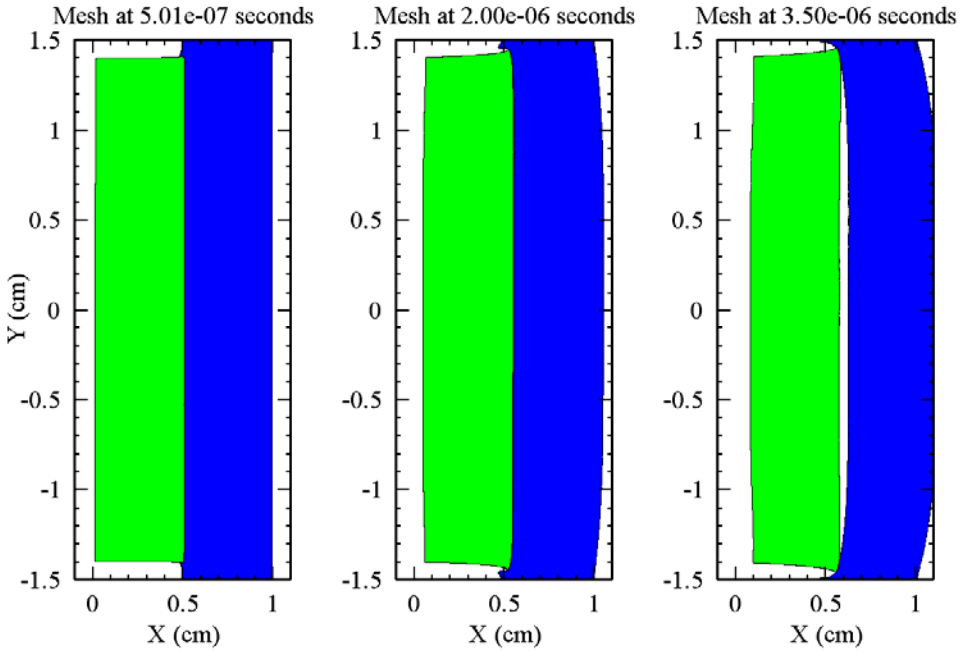

Figure 20 2D CTH viscoelastic model calculation of the high-velocity impact of an aluminium target plate by a steel flyer plate with maximum misalignment gap of 0.05 mm (at y= -1.4 cm) at impact velocity, U_0 = 365 m/s

The first and main case of the present analysis is the simulation of the VISAR commissioning Test 2 with the misalignment geometry shown in Fig. 11(*b*) and corresponding to that from the previous calculation. The calculations in this section have mainly been conducted on a fine mesh, $\Delta x = 1.25 \cdot 10^{-2}$ mm, providing a converged solution. The effect of the grid size on the results will be addressed briefly later in the subsection.

The material boundaries and pressure contours within the flyer plate-target assembly for this simulation are shown in Figs. 20 and 21, respectively. It is seen from Fig. 20 that the flyer plate tilting that corresponds to $\Delta_0 = 0.05$ mm (the schematic of this geometry is shown in Fig. 11(*b*)) is hardly noticeable for the 28 mm diameter (width in the 2D-case), 5 mm thick flyer plate. However, the tilting has quite a noticeable effect on the pressure distribution when the shock waves propagate in the target and flyer plates, as seen in the first pressure plot of Fig. 21 at t = 0.5 μs. These non-parallel shocks continue the non-planarity effect later in time when reflecting from the free surfaces at t = 1.5 μs (second pressure plot) and interacting with the

lateral rarefaction waves. The interaction results in asymmetric pressure zones seen at $t = 3$ μs (third pressure plot) following the flyer-target separation at approximately $t = 2$ μsec.

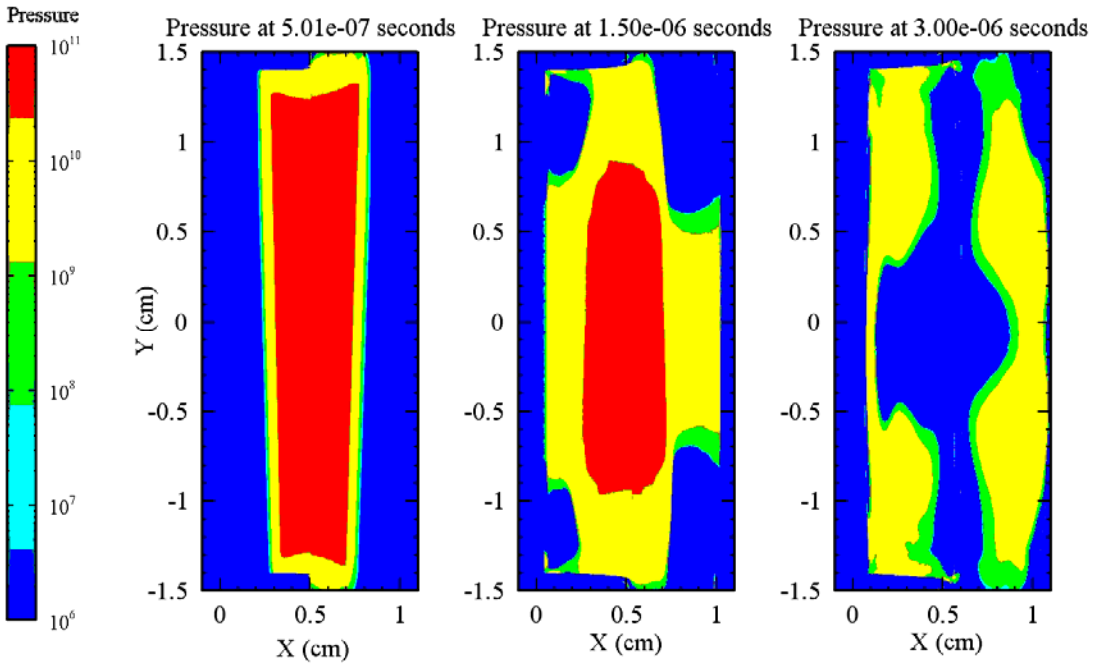

Figure 21 The pressure distributions in the flyer plate-target assembly for the misaligned set-up of Fig. 11(b)

To observe the effect of tilt on the velocity tracers, a control calculation has also been conducted with an idealised flyer plate-target alignment ($\Delta_0 = 0$). Lagrangian tracers were set up along the x-axis ($y = 0$ line) at the same locations as in the previous subsections with the notations as tracer 1 (tracer M in the middle of the target at $x = 7.5$ mm at the start of the calculations), tracer 2 (at $x = 9.9$ mm or 0.1 mm from the free surface of the target), and tracer 3 (tracer V on the free surface of the target at $x = 10$ mm at the start of the calculations).

Velocity tracers M and V for the 2D CTH calculations of the impact of a steel plate against aluminium 6061-T6 target at $U_0 = 365$ m/s are shown in Fig. 22 for the case of the aligned (Fig. 22(p)) and misaligned (Fig. 22(q)) geometries. The results appear to be very similar; however, there are some differences in the vicinity of the elastic precursor.

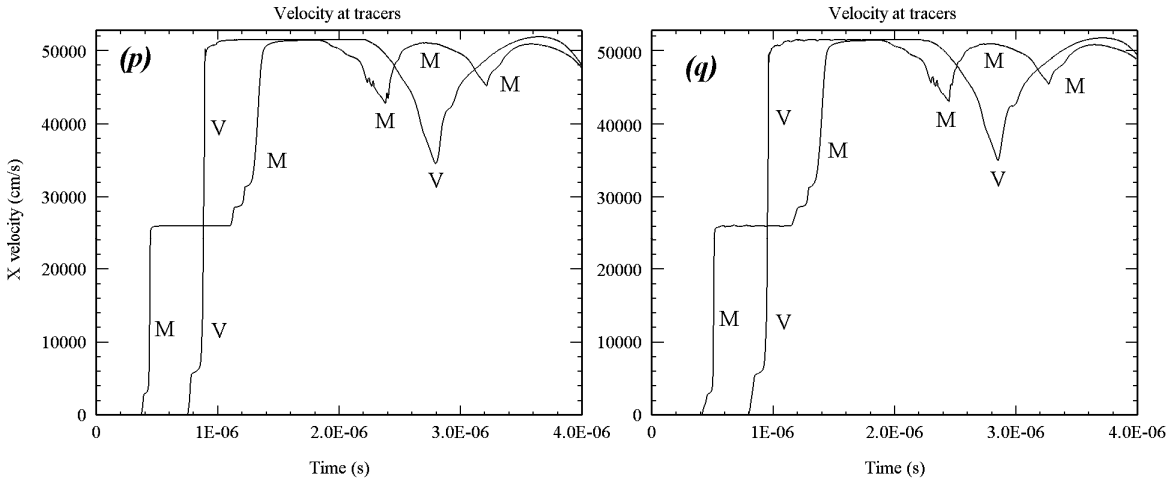

Figure 22 Velocity tracers in the middle (M) and at the free surface (V) of the target from the two-dimensional CTH calculations with aligned (p) and misaligned (q) set-ups

To examine this difference we enlarge the elastic precursor region and analyse the results for all three tracers (including the one at 0.1 mm from the free surface). These detailed views are shown in Fig. 23 as profiles *p*, for the aligned geometry, and profiles *q*, for the geometry with misalignment $\Delta_0 = 0.05$ mm (see Fig. 11(*b*) for the set-up details).

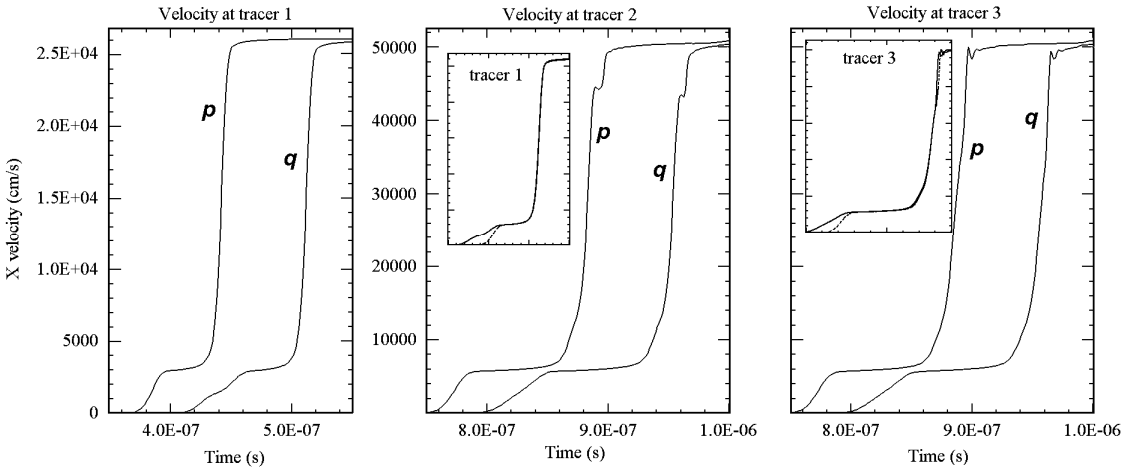

Figure 23 Velocity tracers for the aligned (p) and misaligned (q) flyer plate-target geometries. The velocity tracer 2 at 0.1 mm from the target's free surface illustrates the numerical effects of the Eulerian calculations.

The first difference observed in Fig. 23 is the variation in the time of arrival of the elastic and plastic waves. It should be noted that this difference is mainly caused by the introduced shift of the projectile centreline point (the point at the impacting surface of the projectile at $y = 0$) by $\Delta_0/2$ for the case of the tilted projectile. For $\Delta_0 = 0.05$ mm, the contact of the projectile with the target at $y = 0$ occurs at $t = \Delta_0/(2U_0) = 0.025/0.365$ μs ≈ 0.068 μs. When adjusting the profiles *q* by a time shift of 0.068 μs and superposing them over the dashed profiles *p*, the plastic waves are almost coincident. This is shown in the insert plots for tracer 1 and tracer 3 in Fig. 23. Thus,

the time of arrival difference for the plastic waves at the centreline is simply an earlier start of the calculation for the tilted flyer plate due to an earlier arrival of the upper corner point contacting the target. Thus, the primary conclusion from this comparison is that the tilt condition does not have a major effect on the main shock wave, but it does affect the elastic precursor. The second difference is that the time of propagation of the effective elastic precursor is longer for the case of the tilted projectile than for the perfectly aligned impact. This extra length is associated with the wave splitting of elastic precursor into a two-wave structure. The nature of this phenomenon will be discussed in more detail below.

One more analysis that can be made from Fig. 23 regards the numerical accuracy of the wave resolution. It is seen from the profile *q* of tracer 1 that the elastic precursor has a clear two-wave structure. However, when the precursor reflects from the free surface the two-wave structure is considerably smeared, appearing as a longer shallow front of the precursor. When comparing the calculations for tracer 2 and tracer 3 it is seen that the precursor is not the only wave suffering from the material-void interface erosion effect. The plastic shock also has some numerical features associated with the erosion that are consistent with both the planar and misaligned geometries.

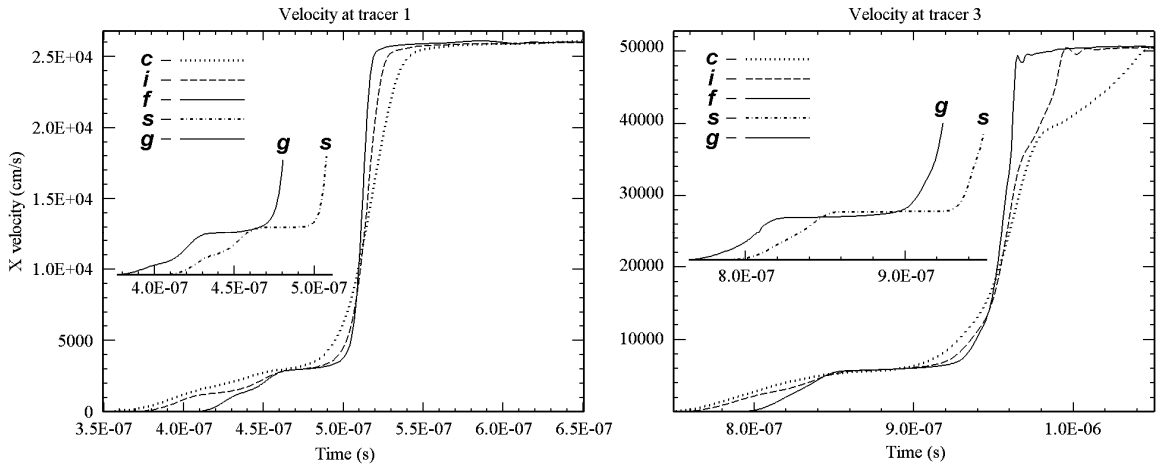

Figure 24 Velocity tracers in the middle (tracer 1) and at the free surface (tracer 3) of the target for calculations performed on a coarse (c), intermediate (i), and fine (f, s, g) mesh. Calculation (g) has been conducted for the asymmetrical geometry and calculation (s) for the misaligned geometry using the SGL model [8].

The influence of the numerical accuracy on the tracers in the middle and on the surface of the target is considered in Fig. 24. The profiles *c* (coarse), *i* (intermediate) and *f* (fine) are obtained on three different meshes using the VEM model in the CTH calculations. These different meshes correspond to grid sizes of $1.25 \cdot 10^{-2}$ mm, $2.5 \cdot 10^{-2}$ mm, and $5 \cdot 10^{-2}$ mm, respectively. It is seen in the coarse mesh calculation that the elastic precursor is smeared in tracer 1 and the reflected plastic wave in tracer 3 is eroded significantly. Thus, the coarse mesh calculation and, moreover, the 3D calculations on a coarse mesh are not capable of resolving the wave features created by the misalignment. Thus, only calculations with the grid size on the order of $1.25 \cdot 10^{-2}$ mm are able to resolve the wave features associated with the projectile-target misalignment.

To determine if the features observed are not a result of the material model used, another material model capable of describing the elastic-plastic effects was also been used to analyse the misaligned geometry. The Steinberg-Guinan-Lund (SGL) model [8] can describe both elastic-plastic and strain rate effects. However, the material constants used in CTH for Stainless Steel 21-6-9, the flyer plate material, and for aluminium 6061-T6, the target material, are given as materials with constant yield stresses independent of strain rate. The tracers for this calculation on the fine mesh are shown in Fig. 24 as *s*-profiles, in the inset, showing only the area of interest in the vicinity of the elastic precursor. It is seen that both the general view (including the time of arrival of elastic and plastic waves) and the two-wave splitting structure of the elastic precursor, due to the flyer-target misalignment for the SGL calculation, are described similarly to the calculation depicted by the *f*-profiles. The only noticeable difference is the strain rate insensitivity, seen as a constant state behind the front of the elastic precursor, instead of the slightly evolving state along the precursor, evident in the previous calculations. To observe if the precursor splitting is specific only to the geometry shown in Fig. 11(*b*), another calculation was conducted with an asymmetrical geometry corresponding to the configuration of Fig. 11(*c*). With this geometry, an asymmetry is introduced by selecting the initial contact point with the target below the symmetry axis of the flyer plate, using a quarter of the flyer plate width and taking $\Delta_l = 0.025$ mm and $\Delta_u = 0.05$ mm. The results of this calculation, performed with the implemented model, are shown as *g*-profiles in the inset of Fig. 24, showing only the elastic precursor area of interest. The full profile is virtually identical to the calculations performed on the fine mesh, profile *f*, and so is not shown. Splitting of the precursor is obvious, with slightly different amplitude of the foregoing wave in front of the elastic precursor. It is interesting to note that in the symmetrical case of the configuration in Fig. 11(*c*), the splitting structure annihilates and degenerates into a single precursor. This confirms that unbalanced wave interference is the main source of the extra splitting.

Obviously, the interference pattern of interest is in the elastic range. The nature of the elastic precursor splitting is mostly substantiated by the evolution of the shear stresses behind the elastic wave front [14]. Therefore, we trace the shear stresses, which are mainly characterised by the deviatoric stresses in the multi-dimensional case. The interference pattern is based on fluctuations of fairly small amplitude, as seen from the velocity tracers in the calculations above. The shear stress fringes for the CTH calculation on the coarse mesh, (profiles *c* in Fig. 24) are shown in Fig. 25. The interference due to the misalignment is noticeable even for the coarse mesh case (Fig. 25(*a*)) but cannot be clearly quantified due to the small interference-to-maximum amplitude ratio. Therefore the colour representation of the deviatoric stresses has been graphically processed, with the stress gradients contoured. The gradient contours corresponding to the intermediate (Fig. 25(*b*)) and fine meshes (Fig. 25(*c*)) are now clearly seen and the periodicity in the structure demonstrates the wave circulation within the elastic precursor. Pressure (more precisely, the stress component normal to the interface) and velocity are the only parameters that are continuous through the material interface. In contrast to this, the shear stresses are different across the material interface for different materials. Therefore, the shear stress gradients in the projectile area are not seen for the chosen stress level to be visualised in the target (Fig. 25).

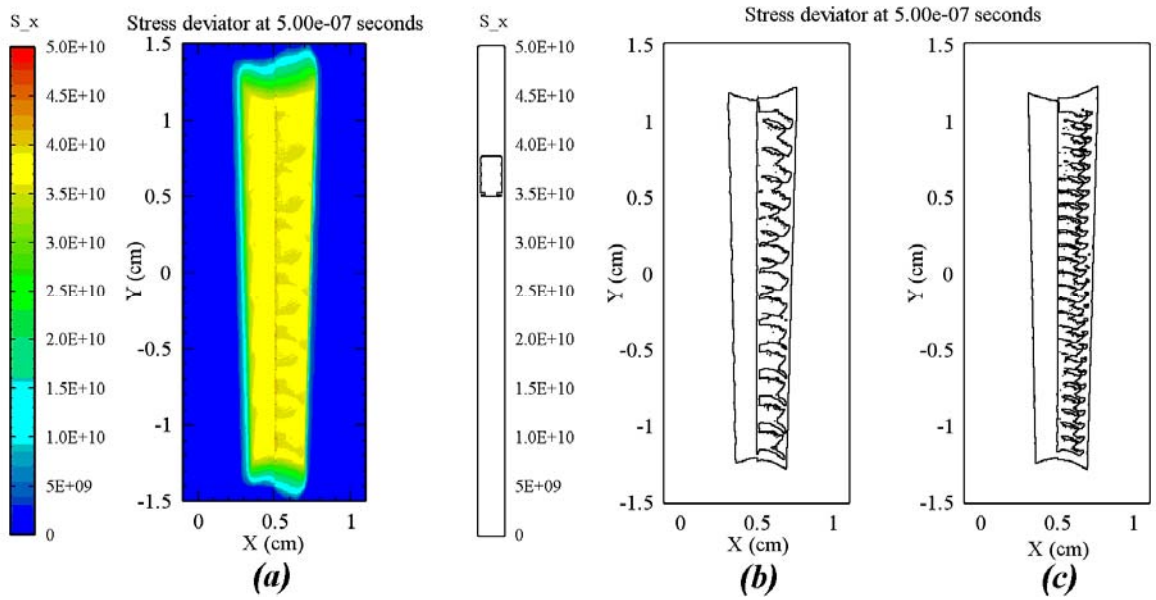

Figure 25 2D CTH calculations showing shear stresses in the target for coarse (a), intermediate (b), and fine (c) meshes. The plots (b) and (c) are graphically processed by contouring the stress gradients.

To assess if the precursor splitting effect is not specifically assembly related, the numerical calculation for Test 1 has been conducted on the same fine mesh with the same misalignment arrangements as for the baseline calculation (configuration in Fig. 11(*b*) with $\Delta_0 = 0.05$ mm). The velocity profiles for tracers 1 and 3 are shown in Fig. 26. They demonstrate the same splitting effect with the same accuracy issues due to material erosion at the free surface, as in the previous calculations.

The calculated free surface velocity should be approximately equal to the impact velocity for an aluminium-aluminium symmetric impact. However, the calculated maximum velocity of the free surface that is close to the impact velocity of $U_0 = 382$ m/s in Test 1, is below the measured free surface velocity of almost 400 m/s in the experimental VISAR record of Fig. 7. This discrepancy can be explained by either mechanical or physical effects. The mechanical effect appears as the continued acceleration of the sabot-projectile assembly through the velocity meter, resulting in an underestimation of the actual impact velocity. The physical effect is the discrepancy between the rarefaction Poisson adiabat in the target material (P_T in Fig. 9) and the shock Hugoniot (H_F that is an exact mirror image of H_T in Fig. 9 for the same flyer plate and target materials). For weak shock waves, the elasticity effect (the strength effect) appearing as the Hugoniot Elastic Limit (HEL) in Fig. 9 in the elasto-plastic materials, which depends on the shock strength, is more significant. The Poisson adiabat P_T is frequently treated as the mirror image of the Hugoniot H_T (coincident with H_F for the same F and T materials) when interpreting experiments. However, this assumption is only an approximation and is better suited to interpreting strong shocks. The physical effect might be less important for Test 2. This is because the steel projectile has greater mass than the aluminium projectile (23.42 g and 8.05 g, respectively) which may reduce any uncertainty in the velocity measurement and hence free surface velocity. The steel-aluminium impact results in a relatively strong shock and therefore the physical effect is also diminished. However, the

latter effect is less likely because the CTH calculation should generally take into account the shock-rarefaction adiabat asymmetry.

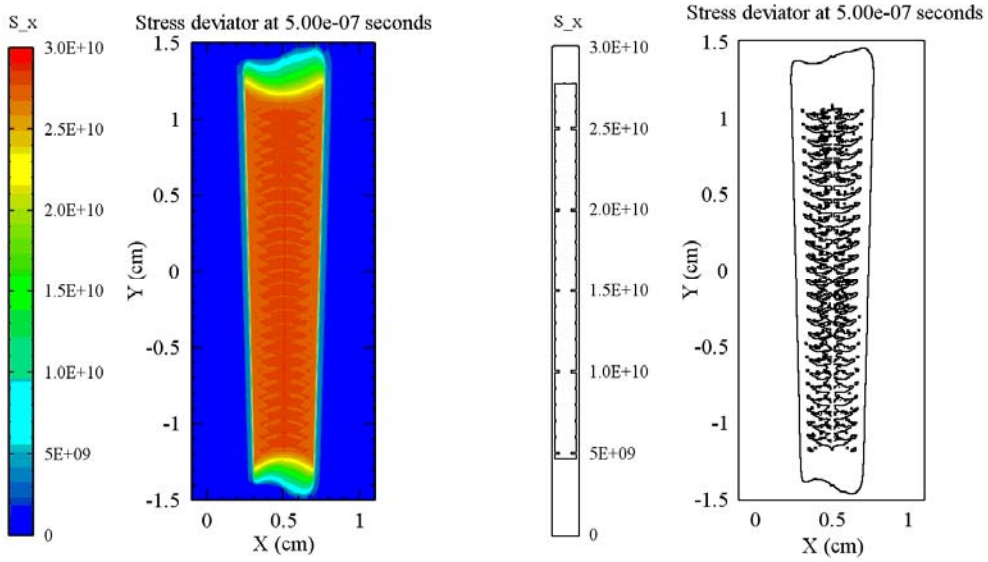

Figure 26 2D calculation of the high velocity impact of an aluminium target by aluminium flyer plate at impact velocity, U_0 = 382 m/s - shear stress and the same plot processed graphically

A similar periodicity, as in the previous calculation, is observed for the stress deviator in the present case (Fig. 27). In this case, the pattern is seen to be continuous through the projectile-target impact interface, because flyer plate and target have the same strength characteristics.

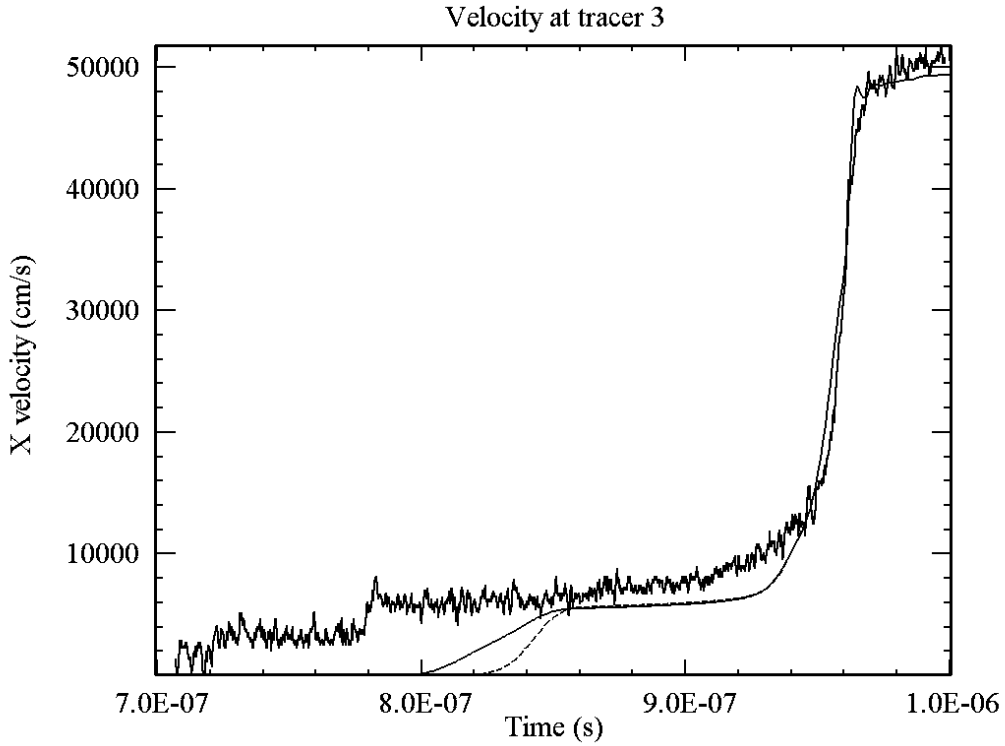

Figure 27 Comparison of the experimental VISAR record with the two-dimensional calculations. The free-surface tracers for misaligned (solid line) and aligned (fragment of the dashed contour adjusted in time to the shock front) set-ups for an aluminium target impacted by a steel flyer plate at the impact velocity of U_0 = 365 *m/s.*

Turning our attention to the experimental results, a portion of the VISAR record from Fig. 10 magnified over 300 ns is shown in Fig. 28. This region shows the split precursor wave and the head of the plastic wave compared with two numerical results. The calculations were performed on a fine mesh. The dashed line represents the aligned geometry and the solid line represents the misaligned case. Both lines represent the free surface velocity. The comparison demonstrates a few features associated mainly with the elastic waves. Moving away from the plastic wave, the experimental profile behind the elastic precursor shows a noticeable receding character. This confirms a noticeable strain rate sensitivity of the target material that maybe even more significant than assumed in the simulation, and certainly more significant than in the *s*-profiles in Fig. 24 where the state behind the precursor is nearly constant. Secondly, the elastic sound speed seems to be slightly higher than in the equations of state used in CTH for both SGL and VEM models. This difference might be caused by specific rolling or other manufacturing conditions for the specimens used in the experiments. Thirdly, there is a clear splitting of the precursor in the experimental profiles and the precursor splitting seen as the smearing in the calculation for the misaligned geometry. The associated accuracy issue has been discussed above in detail and is linked to the material erosion at the free surface interface, which is a numerical artefact.

From the velocity tracers in the middle of the target shown in Figs. 23, 24 and 26 it is seen that, at a sufficiently accurate mesh resolution, the two-wave structure of the precursor can also be simulated for the misaligned geometry. Moreover, depending on the character of the

asymmetrical interaction of the projectile and target, the length and splitting character may vary at different misalignment configurations, as seen from the *g*-profiles of the velocity tracer in Fig. 24.

5. Conclusions

The DSTO VISAR equipment has been commissioned and an operating technique established to measure preliminary high-velocity impact tests using the DSTO small gas gun have demonstrated a new capability in DSTO.

The experimental velocity profiles at the impacted target's free surface have confidently demonstrated the conventional elasto-plastic two-wave shock structure with an evolving elastic precursor confirming a strain rate effect in the target material.

An additional splitting of the elastic precursors has been observed that was attributed to the flyer-plate target misalignment or target surface defects. Two-dimensional CTH calculations using a strain rate sensitive model have confidently demonstrated that the precursor splitting can be caused by the geometry misalignment or surface imperfections. The 2D calculations could not model all misalignment effects but even a basic one-degree of freedom misalignment was able to confirm that the misalignments may introduce additional wave splitting of the precursor wave.

The work conducted has confirmed that the installed VISAR system is suitable and ready for use in material testing and weapons effects studies with time resolution of tens of nanonseconds.

Further work with the VISAR system is aimed at testing advanced materials with a gas gun of a higher bore diameter and launching pressure capacities and improving the quality of the velocity records. Particular emphasis will be focused on development of experimental test set-ups and techniques which will provide better flyer plate-target alignment.

Acknowledgment

The authors wish to thank the New Air Combat Capability (NACC) project for their funding support; Michael Coates for his work as a summer vacation student on the design of the advanced gimble target rig; and Wendy and Zane Barker of Valyn VIP for their assistance with the VISAR system installation and operational training.

References

1. Barker L.M., Barker V.J., Barker Z.M., and Barker W.S., "Valyn VISARS User's Handbook", VALYN International, Albuquerque, New Mexico, USA, 2009.
2. Resnyansky A.D., Bourne N.K., Millett J.C.F., and Brown E.N., Constitutive modeling of shock response of polytetrafluoroethylene, J. Appl. Physics, 2011, v. 110, n. 3, pp. 033530-15.
3. Bell R.L., Baer M.R., Brannon R.M., Crawford D.A., Elrick M.G., Hertel E.S. Jr., Schmitt R.G., Silling S.A., and Taylor P.A., "CTH user's manual and input instructions version 7.1", Sandia National Laboratories, Albuquerque, NM, 2006.
4. Godunov S.K. and Romenskii E.I., "Elements of Continuum Mechanics and Conservation Laws", Kluwer Academic Publ., N.Y., 2003.
5. Resnyansky A.D., Thermodynamically Consistent Decoupled Shear-Volumetric Strain Model and CTH Implementation, Report DSTO-TR-2299, DSTO, Edinburgh, Australia, 2009.
6. Bourne N., "A Test Device for Vulnerability Assessment", Magis Ltd., Swindon, UK, 2001.
7. Grunschel S.E., Experimental procedure for pressure-shear plate impact experiments, informal/draft report, Army Research Laboratory, 2010.
8. Steinberg D.J., Cochran S.G., and Guinan M.W., A constitutive model for metals applicable at high-strain rate, J. Appl. Phys., 1980, v. 51, n. 3, pp. 1498-1504.
9. Resnyansky A.D., DYNA-modelling of the high-velocity impact problems with a split-element algorithm, Int. J. Impact Eng., 2002, v. 27, n. 7, pp. 709-727.
10. Merzhievsky L.A. and Resnyansky A.D., Dislocation structure in the models of dynamic deformation and fracture of metals, J. de Physique, 1985, v. 46, Suppl. n. 8, Coll C5, pp. 67-72.
11. Resnyansky A.D., CTH Implementation of a Two-Phase Material Model With Strength: Application to Porous Materials, Report DSTO-TR-2728, DSTO, Edinburgh, Australia, 2012.
12. Brannon, R.M. and Wong, M.K., MIG version 0.0 model interface guidelines: Rules to accelerate installation of numerical models into any compliant parent code, Sandia National Laboratories Report SAND96-2000, UC-405, Unlimited Release, Albuquerque, NM, 1996.
13. Godunov S.K., Zabrodin A.V., Ivanov M.Ya., Kraiko A.N., and Prokopov G.P., "Numerical Solution of Multi-Dimensional Problems of Gas Dynamics", Nauka Press, Moscow, 1976 (French transl: "Résolution Numérique des Problémes Multidimensionnels de la Dynamique des Gaz", Mir, Moscow, 1979.
14. Merzhievsky L.A. and Resnyansky A.D., Numerical simulation of the shock-wave processes in metals, Combustion, Explosion, and Shock Waves, 1984, v. 20, n. 5, pp.580-587.

DEFENCE SCIENCE AND TECHNOLOGY ORGANISATION
DOCUMENT CONTROL DATA

1. PRIVACY MARKING/CAVEAT (OF DOCUMENT)

2. TITLE

Establishment of a VISAR Measurement System for Material Model Validation in DSTO

3. SECURITY CLASSIFICATION (FOR UNCLASSIFIED REPORTS THAT ARE LIMITED RELEASE USE (L) NEXT TO DOCUMENT CLASSIFICATION)

Document	(U)
Title	(U)
Abstract	(U)

4. AUTHOR(S)

A.D. Resnyansky, S.A. Weckert, A. Foord, and C. Skibinski

5. CORPORATE AUTHOR

DSTO Defence Science and Technology Organisation
PO Box 1500
Edinburgh South Australia 5111 Australia

6a. DSTO NUMBER	6b. AR NUMBER	6c. TYPE OF REPORT	7. DOCUMENT DATE
DSTO-TR-2807	AR-015-538	Technical Report	February 2013

8. FILE NUMBER	9. TASK NUMBER	10. TASK SPONSOR	11. NO. OF PAGES	12. NO. OF REFERENCES
2012/1214662/1	DMO 07/315	DGNACC	29	14

13. DSTO Publications Repository

http://dspace.dsto.defence.gov.au/dspace/

14. RELEASE AUTHORITY

Chief, Weapons Systems Division

15. SECONDARY RELEASE STATEMENT OF THIS DOCUMENT

Approved for public release

OVERSEAS ENQUIRIES OUTSIDE STATED LIMITATIONS SHOULD BE REFERRED THROUGH DOCUMENT EXCHANGE, PO BOX 1500, EDINBURGH, SA 5111

16. DELIBERATE ANNOUNCEMENT

No Limitations

17. CITATION IN OTHER DOCUMENTS Yes

18. DSTO RESEARCH LIBRARY THESAURUS http://web-vic.dsto.defence.gov.au/workareas/library/resources/dsto_thesaurus.shtml

Velocity intereferometry; shock wave; high strain rate; strength effects; hydrocode modelling

19. ABSTRACT

This report describes the establishment of a velocity interferometer measurement system, VISAR, capability in DSTO for recording high-temporal resolution velocity data in high-velocity impact experiments. This data is critical for model validation, material and warhead performance characterisation and effects studies. The present report describes preliminary plane impact tests used to establish the VISAR capability, and evaluates the methodological resolution issues relating to the experimental set-up. The set-up misalignment effects observed on the VISAR records have been numerically analysed using the CTH hydrocode and will be taken into consideration in future test programs.